EUROfusion

WPMAT-PR(18) 19188

Ll M Evans et al.

Image based in silico characterisation of the effective thermal properties of a graphite foam

Preprint of Paper to be submitted for publication in Carbon

This work has been carried out within the framework of the EUROfusion Consortium and has received funding from the Euratom research and training programme 2014-2018 under grant agreement No 633053. The views and opinions expressed herein do not necessarily reflect those of the European Commission.

Image based in silico characterisation of the effective thermal properties of a graphite foam

Ll.M. Evans[1,2,*], L. Margetts[2], P.D. Lee[3], C.A.M. Butler[4], E. Surrey[1]

[1]Culham Centre for Fusion Energy, Culham Science Centre, Abingdon, Oxon, OX14 3DB, UK

[2]School of Mechanical, Aerospace and Civil Engineering, University of Manchester, Manchester, M13 9PL, UK

[3]School of Materials, University of Manchester, Oxford Road, Manchester, M13 9PL, UK

[4]Synopsys, Bradninch Hall, Castle Street, Exeter, EX4 3PL, UK

Abstract

Functional materials' properties are influenced by microstructures which can be changed during manufacturing. Experimental characterisation is often time consuming and expensive. A technique is presented which digitises graphite foam via X-ray tomography and converts it into image-based models to determine properties in silico. By simulating a laser flash analysis its effective thermal conductivity is predicted. Results show ~3% error in two of three planes but is significantly less accurate in the third due to effective thermal conductivity resulting from both the foam's microstructure and graphite's crystallographic structure. An empirical relationship is found linking these by using a law of mixtures. A case study is presented demonstrating the technique's use to simulate a heat exchanger component containing graphite foam with micro-scale accuracy using literature material properties for solid graphite. Compared against conventional finite element modelling these is no requirement to experimentally measure the foam's effective bulk properties. Additionally, improved local accuracy is achieved due to exact location of contact between the foam and other parts of the component. This capability will be of interest in design and manufacture of components using graphite materials. The software used was developed by the authors and is open source for others to undertake similar studies.

[*] Corresponding author. Tel: +44 1235 465213. E-mail: llion.evans@ukaea.uk (Ll.M. Evans).

1 Introduction

Components designed for the nuclear sector (both fission and fusion) are required to withstand challenging environments. Depending on the component's function they may be exposed to extreme environments such as high levels of radiation, temperature, pressure etc. [1]. Future generation nuclear power plants aim to increase output and efficiency over their predecessors, a by-product of which is even more extreme physical operating conditions [2]. In addition to improving engineering concepts; a number of novel materials are proposed which have properties tailored for the specific requirements, these fall into structural [1] and functional [3] categories. In order to achieve their functional specification these materials are often highly anisotropic. Such materials include; foams [4], high entropy alloys [5], MAX phase-materials [6], composites [7], functionally graded materials [8] and nano-grained materials [9].

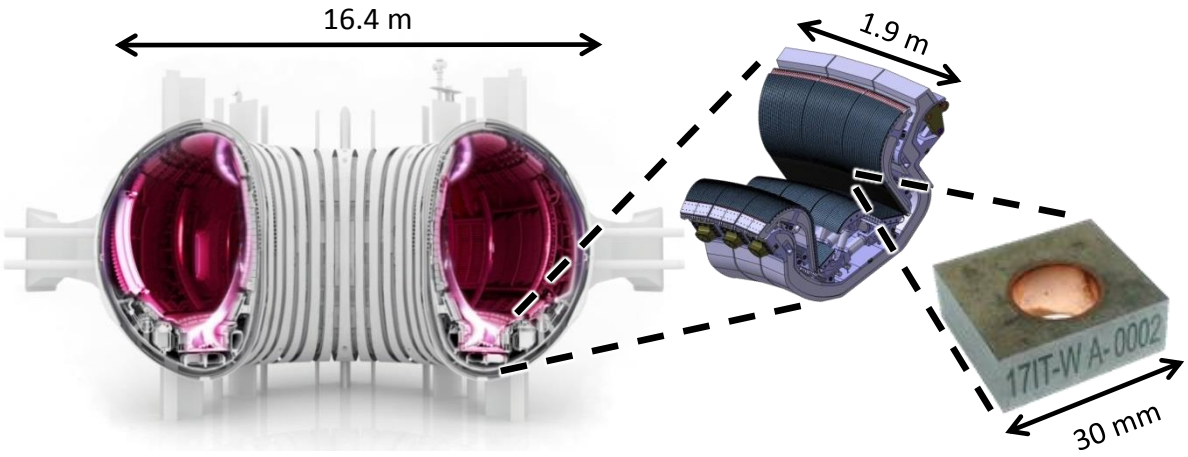

Figure 1. (a) Schematic of a fusion device [1], (b) the divertor region [2], (c) photograph of divertor monoblock (tungsten armour around CuCrZr cooling pipe) which is subject to high heat flux and particle erosion.

In the most common fusion power device, the tokamak, helium, the waste product of the fusion reaction is removed at the divertor by directing plasma along magnetic field lines to strike the divertor target plates. In normal operation this region will experience thermal loads of around 10 $MW \bullet m^{-2}$, as the plasma particle kinetic energy is deposited over the target region [10]. To absorb this energy whilst remaining within operational temperature limits, the divertor design includes active cooling through pipes (built of CuCrZr) protected by tungsten

[1] "The virtual vessel – cutaway with plasma." [Online]. Available: https://www.euro-fusion.org/2011/08/the-virtual-vessel/?view=gallery-11. [Accessed: 25-Jul-2016].
[2] "ITER / Photos / Technical." [Online]. Available: https://www.iter.org/album/Media/7 - Technical. [Accessed: 02-Oct-2017].

(W) armour monoblocks [11]. Figure 1 shows the location of the divertor region within a tokamak and an example monoblock. The armour is bonded to the pipe to maintain thermal conduction, but a large thermal expansion coefficient mismatch between the W and CuCrZr causes high levels of stress within the part. Therefore, a functional interlayer is used at the material interface to create a bond between the pipe and armour with improved longevity. ITER, under construction in France, uses a compliant pure Cu interlayer to relieve stress [12]. In future fusion devices it would be desirable to operate at higher thermal fluxes in the divertor to improve device efficiency, however this would further exacerbate the challenges with thermal stress. Of the various solutions being investigated several candidate designs replace the Cu interlayer with functional materials or geometric constructs [13]. As a result, the performance of these particular designs is highly influenced by micro-scale thermo-mechanical mechanisms.

There is considerable interest in developing capability to engineer micro-structures of graphite foam materials to have specific anisotropic properties capable of addressing this challenge [14]. Typically, the properties of a newly manufactured foam would be characterised by extensive experimental characterisation, requiring many samples to test the range of available orientations [15], [16]. This is usually more time consuming and expensive than the process by which the new foam structure can be created by varying the manufacturing parameters. This is a barrier for rapid development of new graphite foams when attempting to 'tune' the properties to match the desired function of the material. This work considers an alternative method of characterisation by using in silico simulation methods which have the potential to replace experimental methods to reduce time and cost. This is achieved by the use of image-based finite element methods (IBFEM) whereby an X-ray tomography image of the manufactured foam is converted directly into a high-resolution FE model which inherently accounts for the graphite foam's complex microstructure. By simulating the experimental characterisation test (typical of those conducted in the laboratory) we may apply the same conditions and observe the same material response in order to derive a measured property. This may be possible for scenarios where the bulk (or parent) material properties are already known and they are affected significantly by microstructural features caused by the manufacturing process, e.g. a graphite foam material. The additional benefit is that once a block of foam is digitised via conversion from a tomographic image, many samples, e.g. 'dog-bone' for mechanical tensile testing, can be digitally 'cut' from the same block whose volume would overlap in space. If done

experimentally much more material would have to be manufactured to produce a sufficient number of samples, which is a source of variability between tests.

The component which forms the case study presented here is part of a heat exchanger. Because of this. the thermal properties of the graphite foam are of particular interest. There are various experimental methods by which these can be measured. Laser flash analysis (LFA) is one characterisation test which is increasingly being adopted as the standard method for measuring thermal diffusivity (by which thermal conductivity can be inferred). Because LFA is an established and widely accepted experimental technique we will consider image-based modelling this test on foam for this work to predict its thermal properties in silico.

Previous attempts have been made to estimate the effective thermal conductivity of graphite foams analytically using a unit cell model that considered parameters such as porosity, pore diameters and side length of wall [17], [18]. Although these make some steps towards estimating the effective conductivity they do not account for anisotropy. FE analysis has been used to include some effect from anisotropic microstructure [19]. The disadvantages of these approaches is that they are largely idealised forms of graphite foams which do not account for the large variability in pore size or shape distribution and require a substantial knowledge about the foam's microstructure as model inputs.

In this work the graphite foam, KFOAM (Koppers Inc., Pittsburgh, PA, USA), is considered because of its comparatively high thermal conductivity, 240 W/m•K (approximately half that of copper), and diffusivity enables rapid heat dissipation in thermally critical applications. In addition to this, its thermal properties are anisotropic, with thermal conductivity reducing by 75% in one of the orthogonal planes. If utilised correctly, the material micro-structure could be designed to favourably direct the thermal flow through the component to reduce thermally induced stresses. Finally, its inert characteristics mean that it is highly resistant to corrosion in challenging environments.

By using KFOAM as an example, this paper investigates the potential of using image-based finite element method to simulate a standard laboratory test for characterisation of thermal properties. Thus, if the bulk properties of a solid equivalent are already known, it is shown how this technique may be used to significantly reduce and maybe replace experimental testing for similar materials where microstructure dominates the effective material properties. The paper then presents a case study of how IBFEM may be used to virtually analyse the performance of a newly manufactured material used in its desired manner. This is achieved

by digitally ‘cutting’ the manufactured block of graphite foam to the required dimensions to be included within a component. The more conventional materials within the component are added using standard computer aided design (CAD) to produce a hybrid CAD-IBFEM model, a form of digital manufacturing. This method gives an estimate of the in-service behaviour of a novel material can be achieved without experimental work. Additionally, this should produce estimates with a higher degree of accuracy because the complex anisotropic behaviour of the material is inherent to the model instead of using homogenisation methods. The example used in this paper is that of a divertor monoblock (a heat exchange component) for a tokamak, a type of fusion energy device.

2 Material

The graphite foam selected for use was KFOAM P1 HD (Koppers Inc., USA). KFOAM is produced from mesophase pitch which is derived from coal tar. The foaming process was devised at Oak Ridge National Laboratory, USA. The material properties of interest to this investigation, as reported by the material manufacturer[3], are shown in Table 1. The $\perp$ and $=$ symbols denote perpendicular and parallel orientation to the direction of foam ‘growth’ during manufacture. The manufacturer informed the authors that the bottom 3.2 mm of the sample would have a different foam structure as an artefact of the manufacturing process. If the material was to be used, this portion would first need removing.

Table 1. Manufacturer’s values for effective (bulk) properties:

Density	675	kg/m^3
Pore Size Pore Volume	>60	%
Bulk Thermal Conductivity $\perp$	240	W/m·K
Bulk Thermal Conductivity $=$	64	W/m·K
Thermal Diffusivity	369×10^{-6}	m^2/s
Average wall thickness	348×10^{-6}	m

3 Methodology

This section details the methodology for (i) three-dimensional imaging using X-ray computed tomography, (ii) processing of CT image data and conversion into digital geometry (iii) finite element mesh generation, (iv) definition of simulation boundary conditions, equation solution

[3] “KFOAM® | Koppers.” [Online]. Available: http://www.koppers.com/pages/kfoam. [Accessed: 26-Jul-2016].

parameters and results analysis. The following results and discussion sections follow the same format.

3.1 X-ray computerised tomography (CT) scanning

X-ray tomography scanning was performed using a Nikon Metrology 225 kV system at the Manchester X-ray Imaging Facility, Research Complex at Harwell, Rutherford Appleton Laboratory, UK. Imaging and reconstruction parameters are shown in Table 2. The voltage and current parameters relate to the electron gun aimed at a target to produce X-rays. The X-ray signal is passed through the specified filter before being incident on the sample and then detector. During reconstruction, beam hardening occurs when polychromatic beams are used and the soft X-rays (lower energy) are filtered by the sample giving the false appearance of a change in attenuation through the sample. That is, the change in greyscale through the material is not caused by a change in the material (e.g. density) but rather an artefact of the imaging technique. Noise reduction is a standard image processing method that utilises smoothing algorithms. The digital filters used to correct for beam hardening and noise range from 0-5, with 5 being the strongest correction level.

To avoid the release of carbon dust from the sample it was scanned whilst within a sealed plastic bag. The bag is sufficiently transparent to X-rays that it will not adversely affect the imaging. Reconstruction of the 3D volume from 2D radiographs was completed using CT Pro V3.1.4785.19683 (Nikon Metrology NV, Tring, Hertfordshire, UK).

Table 2: X-ray tomography scanning and reconstruction settings.

Scanning						Reconstruction	
Voltage (kV)	Current (µA)	Filter (mm)	Acquisition time (s/projection))	Number of projections	Frames / projection	Beam hardening	Noise reduction
70	143	Al, 2	1	2001	1	0	1

3.2 Image post-processing

CT data output essentially consists of a series of 2D slices, e.g. Figure 12. The sliced data is made up of pixels with an associated greyscale value, giving information about the extent to which X-rays are attenuated in that point in space. In between the slices the data is interpolated to create volumetric pixels, commonly known as voxels. When the slices are stacked together these represent a 3D volume.

Before being able to create an FE mesh the data must go through a ‘segmentation’ process to define which regions or ranges of greyscale values belong to the various materials. To carry out this step the open source software Fiji [20] was used which is a specific distribution of ImageJ [21] which includes plugins specifically to facilitate scientific image analysis. The image was first cropped to remove the sample bag, sample holder and outer air. By use of greyscale thresholding, both foam and porous phases were defined resulting in a binarised 3D volume image.

At this stage the binarised images were analysed to investigate the graphite foam’s structure. The number of voxels belonging to the foam give its volume because the volume of the voxels are known. Using this method it was also possible to quantify the porosity of the material. By using the graphite foam’s measured mass and actual volume it was possible to calculate the density of the carbon itself, in addition to the effective density of the foam.

The lower 3.2 mm of the sample was removed (cropped) as this contained the foam with a different structure due to manufacturing method. The external volume was also cropped to leave only the graphite foam. To investigate the anisotropy in the thermal paths through the graphite foam a skeletonisation process [22] was undertaken on a region of interest (200 x 200 x 200 pixels). The skeletonisation process gradually ‘erodes’ (or thins) the object until its paths are only one voxel in diameter. When these points are connected they create a centreline. This makes it possible to perform analyses on the thermal paths through the foam e.g. lengths and directionality.

From the centrelines generated in the region of interest the graphite foam’s tortuosity was found in a range of planes [23]. The tortuosity, τ, is a ratio of the measured path length, L, to the Euclidian distance, C, (i.e. ‘bee line’) as shown in Figure 2 and Equation (1). By this method it is possible to compare how the tortuosity changes with relation to the foam’s orientation as a measure of the anisotropy. The tortuosity is of interest because the effective thermal conductivity of the material is directly related to how ‘quickly’ heat may transfer from one bounding surface to the other. A longer path may indicate a lower effective thermal conductivity. An ‘image analysis method’ approach has previously been used to obtain shape factors in a metal foam [24]. This was used in a derivation of an analytical solution that included tortuosity as one element of the approach. However, in that instance, the foam was isotropic in its micro-structure.

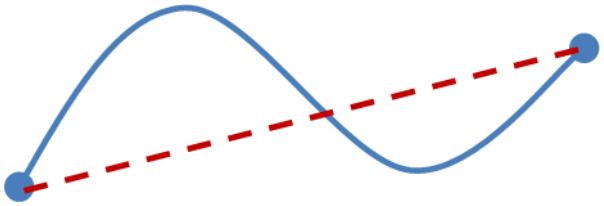

Figure 2. Path length in blue continuous line and Euclidian distance in red dashed line.

$$\tau = \frac{L}{C} = \frac{Path\ Length}{Euclidian\ Distance} \tag{1}$$

3.3 FE mesh generation

To generate the FE meshes the binarised volume images were imported into ScanIP, part of the Simpleware suite of programmes, version 7 (Synopsys Inc., Mountain View, CA, USA). Two sets of meshes were created: a) cylindrical discs as used for laser flash analysis (LFA) experiments and b) fusion divertor monoblock components with a foam interlayer.

Important to the validity of any results calculated by FE is the 'quality' of the elements that make up the mesh i.e. how closely they match the ideal geometry of an equal sided tetrahedron or hexahedron. If elements are highly distorted they are known to cause numerical difficulties, often overpredicting stiffness or resistivity in mechanical or thermal models, respectively. For image-based models this can be particularly challenging because of the non-idealised freeform geometries. Conventional metrics were used to investigate the mesh quality (e.g. ratio of longest to shortest edge length), looking at the mean results and the worst elements.

3.3.1 In silico experiment: laser flash analysis

The LFA cylindrical discs (or pucks) were digitally 'cut' out of the graphite foam block to have a diameter of 12.7 mm and a thickness of 4 mm. Three discs were cut from each orientation (xz, yz and xy), one from the centre of the block and one each side, offset by approximetely 1/4 and 3/4 along the axis of that orientation. Thus there were nine virtual LFA discs in total, as shown in Figure 3 (Xlow, Xcentre, Xhigh, Ylow, Ycentre, Yhigh, Zlow, Zcentre and Zhigh). An example is shown in Figure 4.

In an LFA experiment a laser is pulsed on one surface of the sample while an infrared camera tracks the temperature rise on the opposite surface. If the disc was to be used in an LFA experiment in its current form the laser would interact with the graphite foam at various penetration depths into the sample because it doesn't have a solid upper surface. Similarly the infrared camera would see temperatures at a range of depths through the sample where there is a direct line of sight. In some samples there may be a direct line of sight between the laser and infra-red camera. This would make measuring thermal diffusivity of a foam via LFA extremely challenging. To mitigate this a method was used by Zhao et al. [25] is to sandwich the foam between two solid layers. Therefore, additional thin solid layers of graphite (0.25 mm) were digitally added to the top and bottom of the discs assuming a bond which is in perfect contact with the graphite foam.

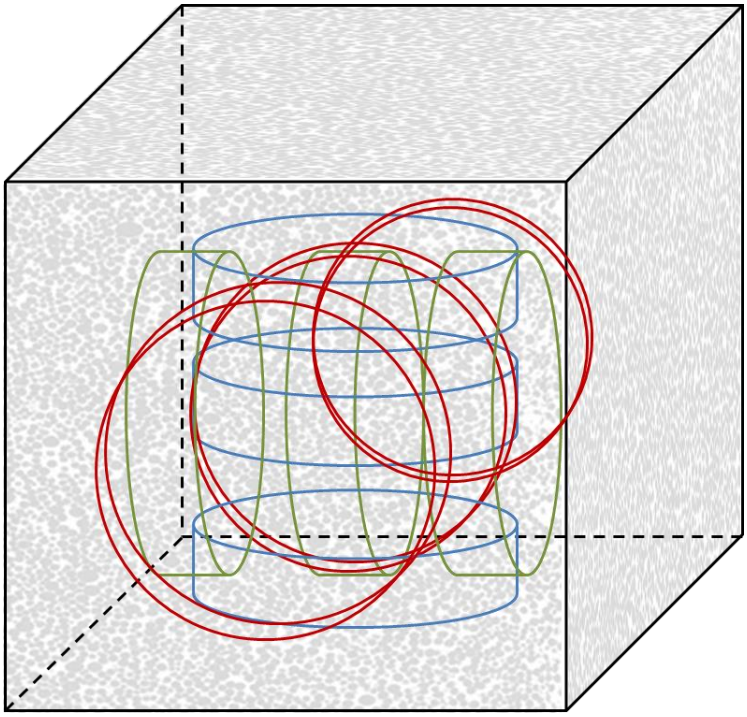

Figure 3. Schematic showing approximate locations of the LFA samples digitally 'cut' from the graphite foam block.

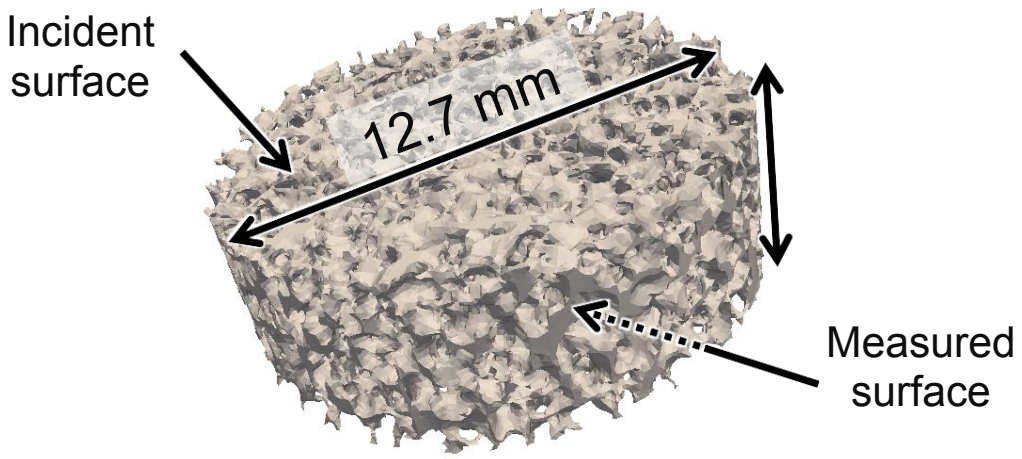

Figure 4. Example virtual LFA KFOAM cylindrical disc digitally 'cut' from larger foam block.

3.3.2 Case study: Fusion energy heat exchanger component

For the monoblock, a ring shaped interlayer section (inner diameter = 12 mm, thickness = 1 mm) was virtually cut out of the digital foam cube and joined to CAD versions of the outer armour (22 mm x 22 mm x 4 mm, central bore with 14 mm diameter bore) and coolant pipe (inner diameter = 10 mm, thickness = 1 mm) to produce a micro-scale accurate virtual monoblock, as shown in Figure 5.

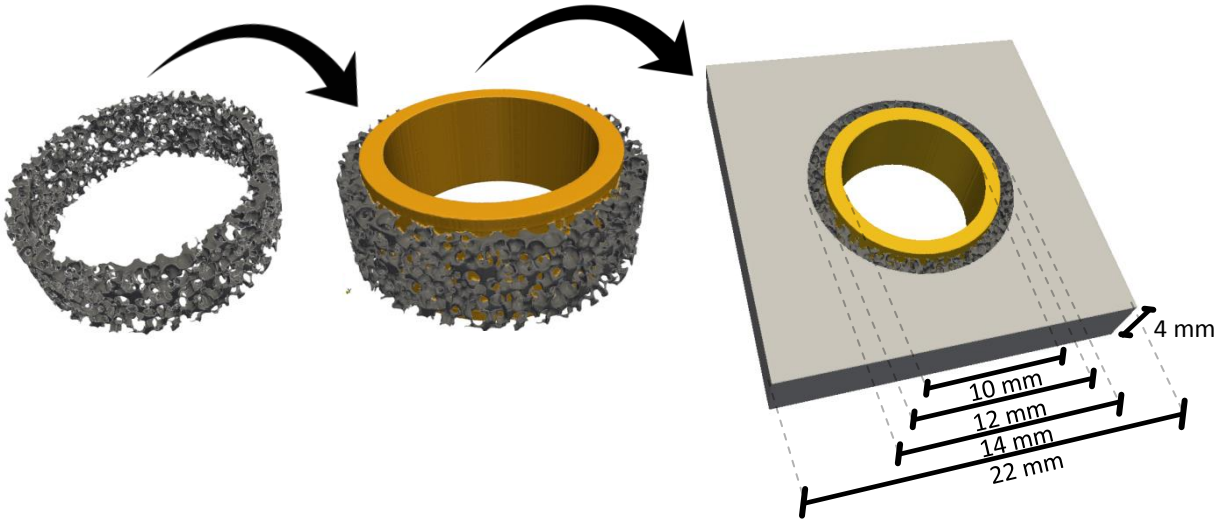

Figure 5. Virtual manufacturing workflow: graphite foam interlayer digitally cut from block, CAD pipe and CAD armour added, respectively.

Once the desired geometries had been constructed they were converted into tetrahedral FEM meshes with sufficiently fine resolution in order to retain the microstructural detail, as shown in Figure 6. Within the Simpleware software the meshing algorithm '+FE Free' was used.

Whilst discretising the surfaces and volumes, this algorithm will decimate using larger elements where possible whilst retaining geometric detail within set error limits. Reducing the total number of elements decreases the computational expense. Through trial and error, a coarseness setting level of -10 and -25 was found to produce a desirable balance between mesh 'quality' and number of elements for the LFA and monoblock meshes, respectively. Details on the resulting mesh quality can be found in the supplementary data section.

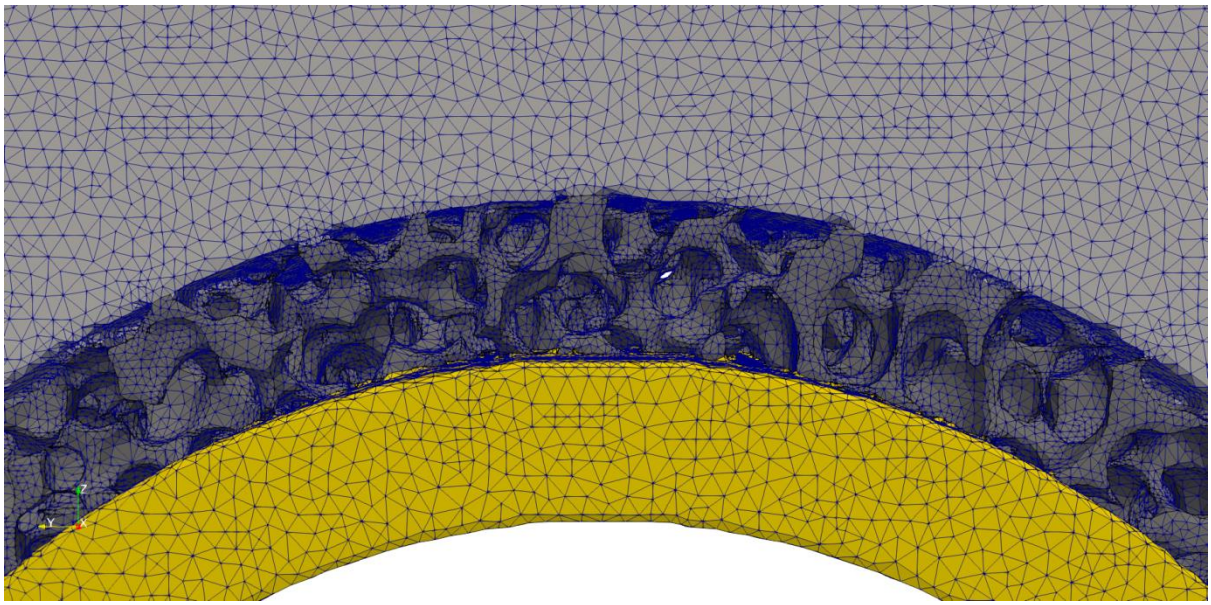

Figure 6. Image showing level of mesh refinement used to accurately retain microstructural detail.

3.4 Simulation

To resolve small-scale features, IBFEM meshes can contain millions of elements compared with tens of thousands usually produced by CAD-based models. This reflects the true topology of complex surfaces (such as foams) that cannot be represented using primitive or simple CAD geometries. When topological detail is required, larger mesh sizes result in more calculations. Commercial FEM software packages cannot solve these large and complex simulations on desktop PCs. Furthermore commercial FEM software is not suited to supercomputers because they do not make efficient use of parallelisation. Therefore, the open source solver ParaFEM, revision 2084 [4], developed by the authors [26]–[28], was used because it has previously been shown to scale well on parallel computing architectures i.e. the time to solve almost halves as the number of computational cores doubles [29], [30].

[4] ParaFEM [r2084] https://sourceforge.net/p/parafem/code/2084.

3.4.1 In silico experiment: laser flash analysis

The required boundary conditions to accurately simulate the laser profile of an LFA experiment have already been discussed in detail by Evans et al. [31], this work uses the same methodology. In brief, a thermal flux pulse is applied to one surface of the disc using a flux load distribution profile as shown in Figure 7 to simulate the laser found in the experimental apparatus. The temperature rise on the opposite surface is tracked with respect to time to measure the half-rise time, $t_{1/2}$. Using the exact same post-processing analysis the half-rise time of the curve is used to calculate the thermal diffusivity, α, of a sample of thickness d, see Eqn. (2). This equation is a simplified version of a more complete mathematical model [32] which accounts for some real world mechanisms not included in these simulations (e.g. emissivity). When combined with density, ρ, and specific heat capacity, c_p, this may be used in turn to calculate thermal conductivity, κ, as shown in Eqn. (3). To further gain confidence in the model, the temperature rise, dT, of the sample may be verified against a calculated value by knowing the applied energy from the laser, Q, and the theoretical mass, m, from its density and volume, V, see Eqn. (4).

$$\alpha = 0.1388 \cdot \frac{d^2}{t_{1/2}} \tag{2}$$

$$\kappa = \alpha \rho c_p \tag{3}$$

$$dT = \frac{\mathrm{Q}}{mc_p} = \frac{\mathrm{Q}}{\rho V c_p} \tag{4}$$

A time dependent heat flow analysis was carried out simulating a 0.252 s duration of the LFA experiment. For increased temporal resolution during periods of high gradients (i.e. near the start of the simulation) a variable time step size was used. Details of how the time step size was varied can be found in Table 3. The Crank-Nicolson time-stepping method was used (i.e. using an equal combination of the forward and backward Euler methods) with an iterative solver tolerance of 1.0×10^{-6}.

Table 3. Time stepping scheme for LFA simulation.

Solution step	Time step interval (s)	Number of time steps
1	0.2000E-06	20000
2	0.4000E-06	20000
3	0.8000E-06	20000
4	0.1600E-05	20000
5	0.3200E-05	20000
6	0.6400E-05	20000

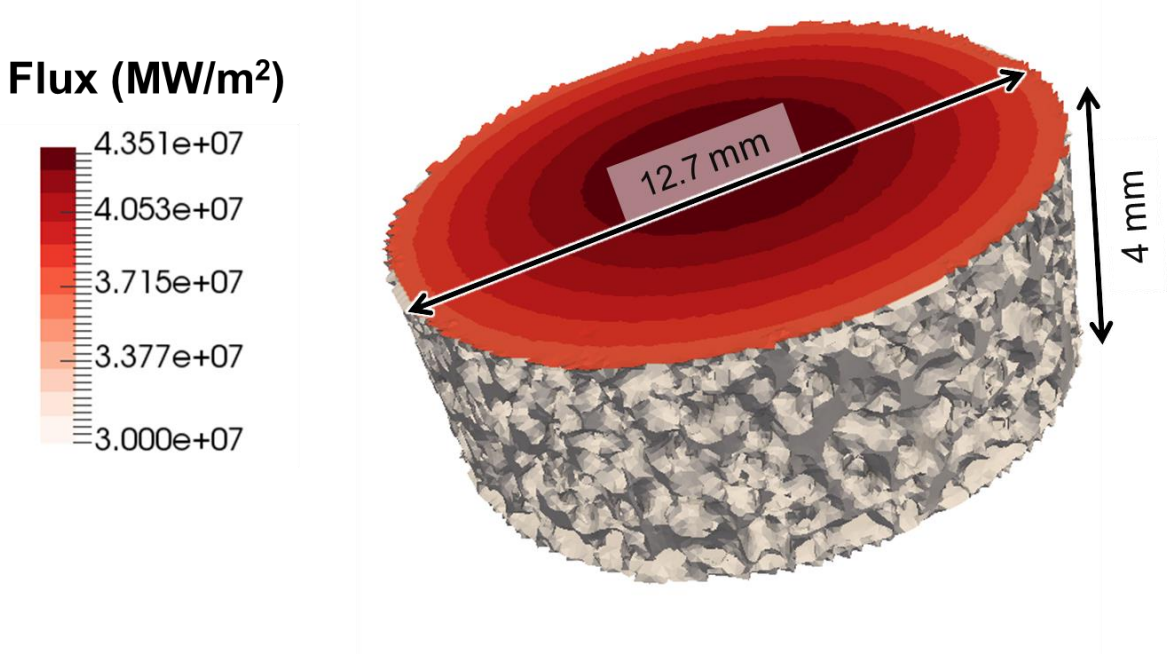

Figure 7. Thermal flux load boundary condition applied to disc samples in LFA experiment simulation.

3.4.2 Case study: Fusion energy heat exchanger component

When modelling the monoblock, boundary conditions were prescribed in such a way to emulate conditions in the divertor region of a fusion device, as shown in Figure 8. These were a global initial temperature of 150 °C, thermal flux of 10 MW•m^{-2} on the plasma facing surface and a fixed temperature of 150 °C on the inner pipe wall due to the water coolant.

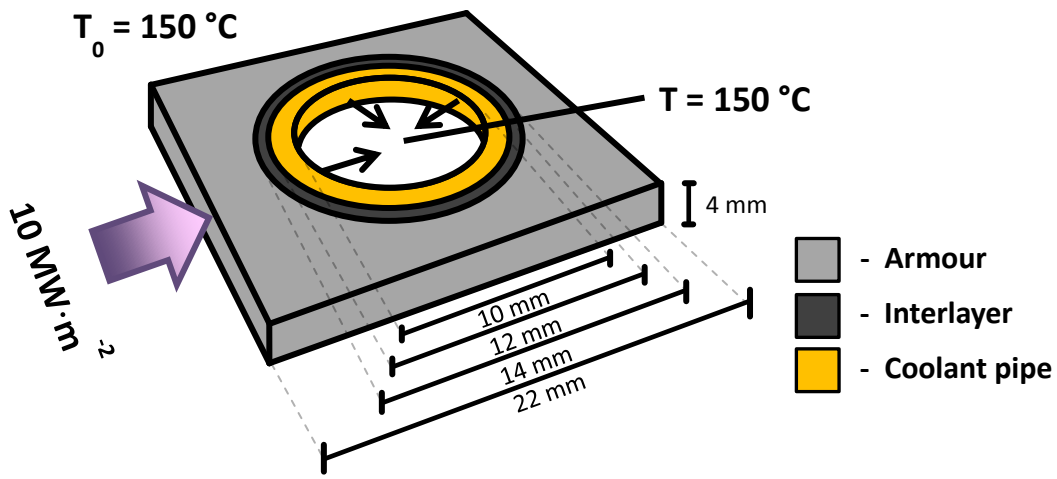

Figure 8. Boundary conditions used to simulate conditions in the divertor region of a fusion device.

A transient heat flow analysis was carried out to determine the time required to achieve a steady state temperature. The same Crank-Nicolson time-stepping method was used as in the LFA simulation. For increased temporal resolution during periods of high gradients (i.e. near the start of the simulation) a variable time step size was also used. Details of how the time step size was varied for this simulation can be found in Table 4.

The LFA simulation included a relatively short transient event, i.e. the laser pulse, and the purpose of that simulation was to accurately measure the travel time the pulse through the sample. Because the monoblock simulation only included steady-state boundary conditions, i.e. the plasma thermal load, it was possible to use fewer time steps with larger intervals to calculate the temperature profile.

Table 4. Time stepping scheme for monoblock simulation.

Solution step	Time step interval (s)	Number of time steps
1	0.000001	100
2	0.00001	190
3	0.0001	180
4	0.001	180
5	0.01	180
6	0.1	30
7	0.5	10

3.5 Material properties

CAD based modelling typically averages localised variations, e.g. caused by microstructure, over a larger volume in a process called homogenisation, e.g. [33], [34]. In a CAD based

model, the graphite foam would be represented by a solid volume representing both graphite and porous phases and be assigned effective material properties. Rather than homogenising, IBFEM modelling represents each distinct phase separately. This investigation presented in this paper uses both CAD and IBFEM simulations. To undertake the range of simulations described in section 3.4 several sets of material properties are required as described below.

For the IBFEM LFA simulations, the material properties of graphite were required which were obtained from literature values [35]. In addition to the anisotropy of the foam microstructure, graphite is a highly anisotropic material on the atomic molecular. Its thermal conductivities are 1950 W/m•K and 5.7 W/m•K parallel and perpendicular to the layer planes, respectively. To investigate the effect of this inherent property two variations of the IBFEM LFA model were used. Firstly, the models were given the literature values for graphite with the alignment matching that of the direction the foam was manufactured. Secondly, an isotropic thermal conductivity was applied in order to have a result that was purely affected by the foam microstructures and not anisotropic properties of graphite. This was averaged from the literature conductivities in the parallel and perpendicular planes, i.e. 978 W/m•K. This arrangement is summarised in Figure 9.

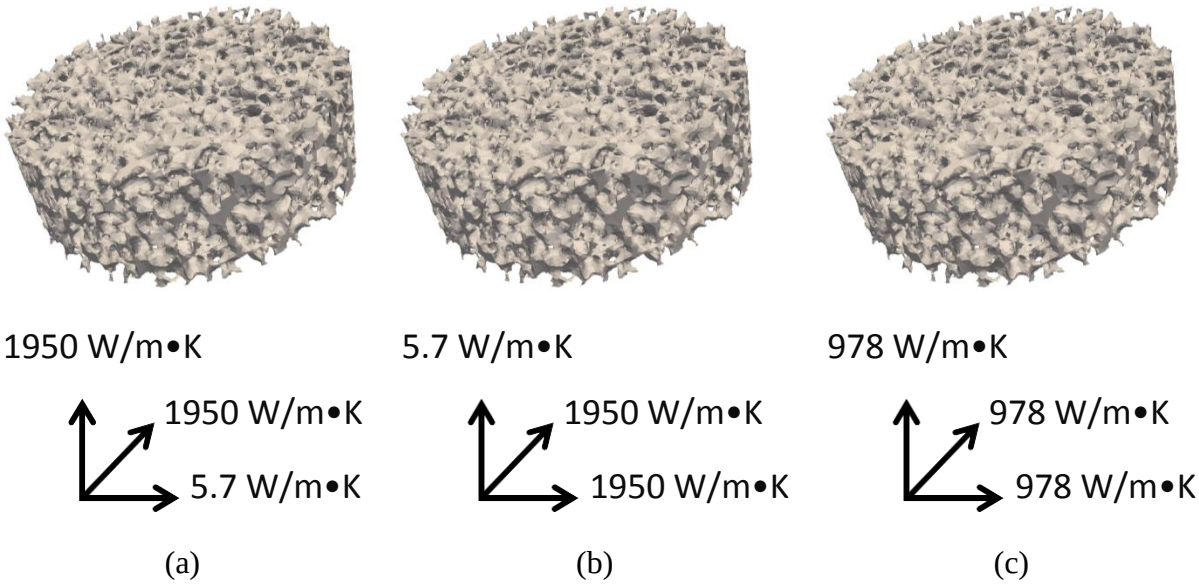

Figure 9. Thermal conductivity alignment used for (a) & (b) $C_{graphite}$ and (c) $C_{avg\_graphite}$.

In addition to the IBFEM LFA models, a homogenised CAD model of a solid disc was solved for comparison. This model was simulated three times a) $C_{foam\perp}$ using the graphite foam manufacturer's homogenised anisotropic material properties (i.e. effective properties measured experimentally, see Table 1) with the laser pulse travelling in the direction where k

= 240 W/m•K, b) $C_{foam=}$ using the same but travelling in the direction where k = 64 W/m•K, c) using $C_{avg\_graphite}$ i.e. where k = 978 W/m•K in all directions. The CAD simulations were performed to demonstrate whether simulating the LFA experiment in this manner is an appropriate method to back calculate the material's thermal conductivity. That is, would the result for thermal conductivity from derived from simulating the experiment match the input value.

For the IBFEM monoblock model the averaged literature values were used so that the result was purely affected by the foam microstructures and not anisotropic properties of graphite. In order to compare with standard CAD practice, the same simulation was repeated twice using homogenised CAD based models. Firstly the $CAD_{anisotropic}$ model used the C_{foam} properties with the plane of lower thermal conductivity aligned in the same direction as the IBFEM model. Secondly the $CAD_{isotropic}$ model used the same $C_{avg\_graphite}$ material properties as the IBFEM model but applied to the homogenised CAD interlayer. This was to create a comparative isotropic baseline to test the sensitivity of the model to changes in thermal conductivity of the interlayer. The values for all the material properties used are shown in Table 5. For consistency and to remove any potential influence of mesh dependency all models used the same mesh geometry i.e. nodal coordinates and element structure. To homogenise the interlayer, the CAD models applied the same material properties to both foam and porous phases. The three variations, i.e. $CAD_{anisotropic}$, $CAD_{isotropic}$ and IBFEM, in assignment of materials to the separate phases are as labelled in Figure 10.

Table 5. Material properties used for modelling.

	Thermal conductivity			Density	Specific heat
	K_x (W/m•K)	K_y (W/m•K)	K_z (W/m•K)	ρ (kg/m^3)	c_p (J/kg•K)
W*	160	160	160	19279	134
CuCrZr*	339	339	339	8840	386
C_{foam}	240	64.0	240	675	964
$C_{graphite}$	1950	5.70	1950	2200	709
$C_{avg\_graphite}^{+}$	978	978	978	2200	709

*Temperature dependent material properties were applied for W and CuCrZr, the values shown in this table are for the initial temperature for a relative comparison with C.
+Thermal conductivity calculated as average from different orientations of graphite as found in literature [35].

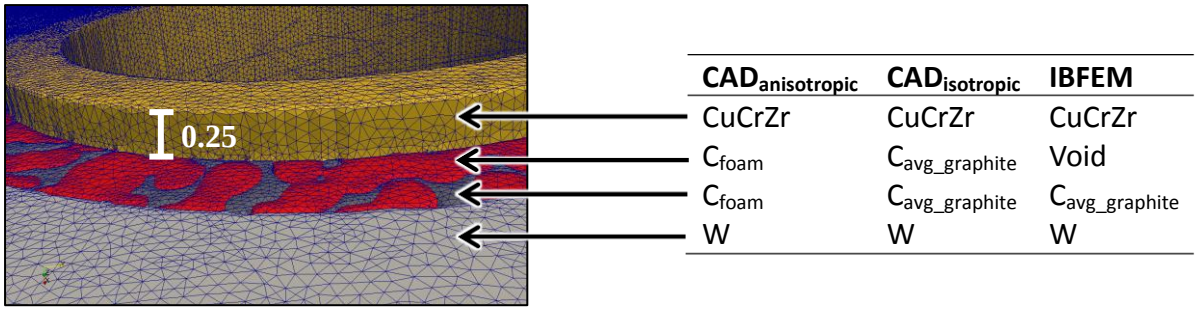

Figure 10. Mesh output from Simpleware, with micro-scale features accurately captured. Also shown are the materials assigned to each phase of the monoblock model for each simulation.

4 Results

4.1 X-ray computerised tomography (CT) scanning

Considering the distances between the cone beam X-ray source, sample and detector a voxel width of 35.4 µm was achieved. An annotated example tomography slice is shown in Figure 11.

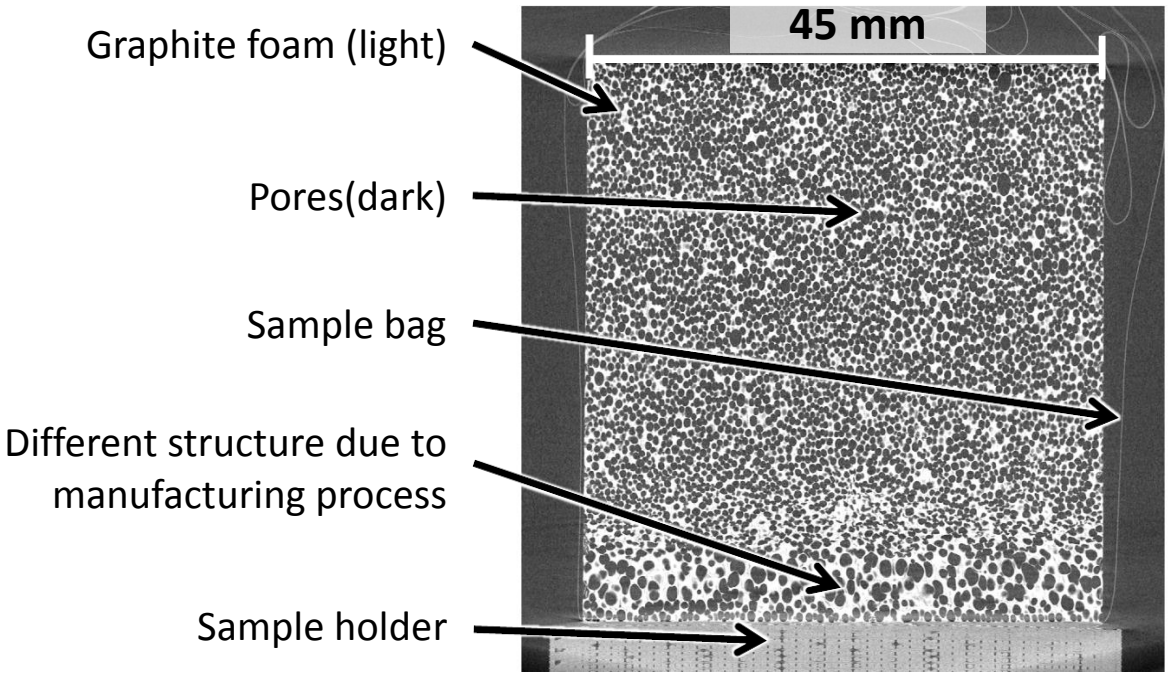

Figure 11. X-ray tomography slice of graphite foam.

4.2 Image post-processing

An example tomography slice showing the steps from greyscale to binarised to skeletonised image is shown from the region of interest in Figure 12. The skeletonised form is more easier viewed in 3D, which is shown in Figure 13.

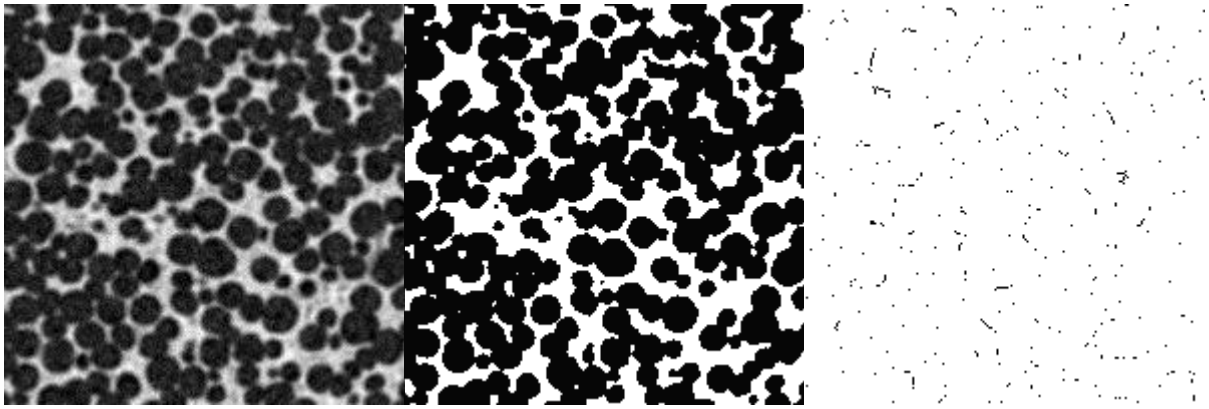

Figure 12. Slice from a region of interest within the graphite foam showing (a) X-ray attenuation map (b) binarised image from thresholding (c) skeletonisation of 3D structure.

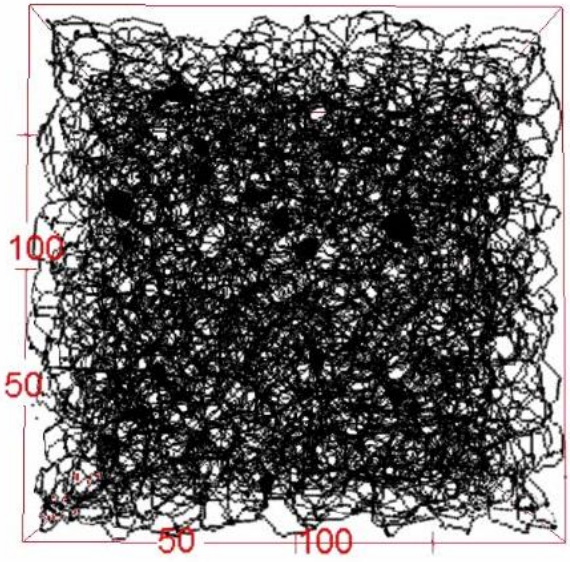

Figure 13. 3D visualisation of the skeletonised region of interest from the graphite foam.

The sample's external dimensions and mass, m, were measured with a micrometre and a digital balance, respectively. The external volume, V, and effective density, ρ, were calculated from these values (i.e. V = h x w x d and ρ = m / V). Despite the inclusion of the 3.2 mm layer at the bottom, the calculated value of 671 kg/m^3 is relatively near the manufacturer's value of 675 kg/m^3. These results are shown in Table 6.

The actual volume of a region of interest from the graphite foam, rather than external sample volume, was measured from the segmented image. This was found to be 2.72 x 10^{-5} m^3. By also knowing its external dimensions it was possible to calculate the sample's porosity and the density of the graphite. These are also shown in Table 6 along with the manufacturer's value for porosity and a literature value for the density of graphite [35].

Table 6. Metrology of graphite foam sample as stated by the manufacturer, measured externally and by analysis of X-ray tomography image.

	Foam (Manufacturer)	Sample (Effective)	Region of interest (Graphite)	Graphite (Literature [35])
Dimensions		0.044 x 0.044 x 0.045 m		
Mass		0.0585 kg		
Volume		8.71 x 10^{-5} m^3	2.72 x 10^{-5} m^3	
Porosity	> 60 %		68.8 %	
Density	675 kg/m^3	671 kg/m^3	2151 kg/m^3	2200 kg/m^3

The variation in tortuosity with respect to changing orientations in θ and ϕ, as defined in Figure 14, as measured via the skeletonisation of a region of interest is shown in Figure 15 and Figure 16. For comparison with the orientations used by the manufacturer for measuring thermal conductivity, the tortuosity in the xz, yz and xy planes are given in Table 7.

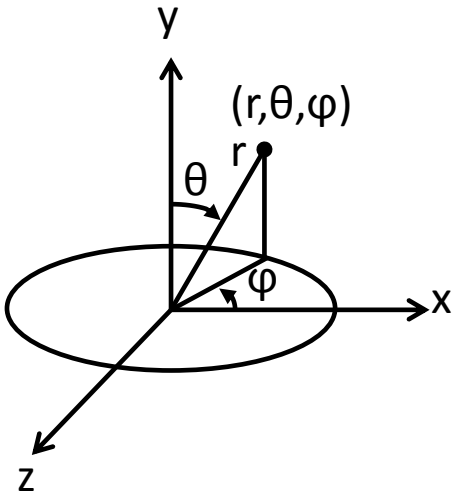

Figure 14. Naming convention used for Cartesian and spherical systems.

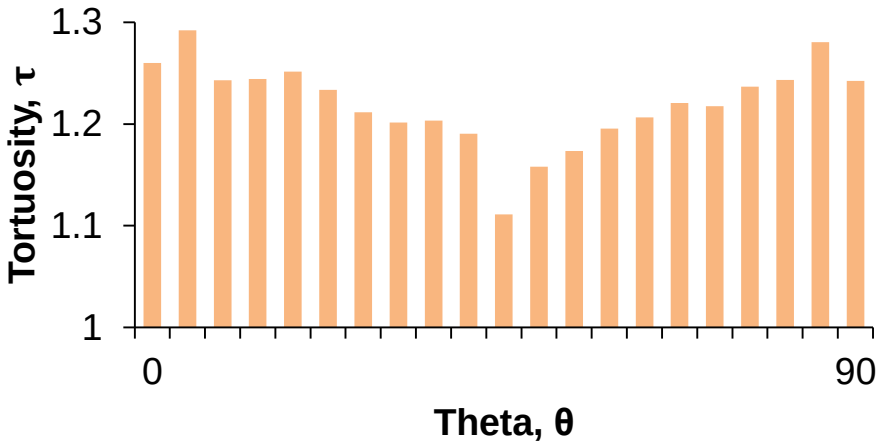

Figure 15. Variation in tortuosity along the path through the graphite foam with respect to θ.

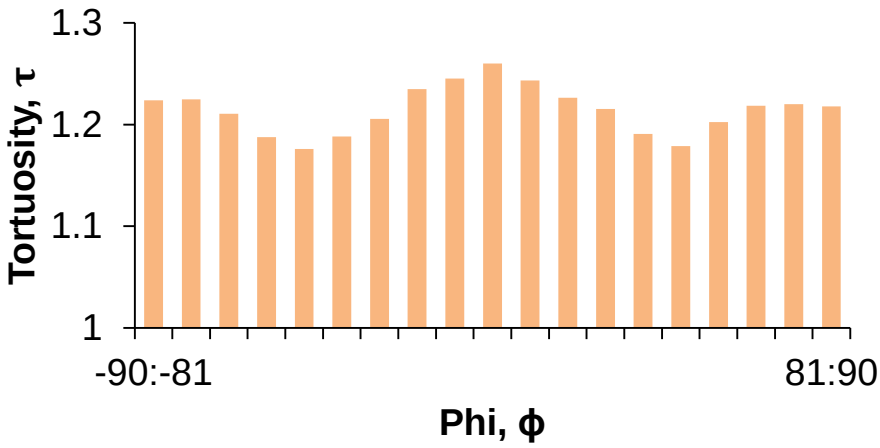

Figure 16. Variation in tortuosity along the path through the graphite foam with respect to ϕ.

Table 7. Variation in tortuosity along the path through the graphite foam in line with the Cartesian axes.

Plane	yz	xz	xy
τ (average)	1.38	1.46	1.36

For the hybrid CAD-IBFEM monoblock model an additional variable is introduced in the form of converting CAD drawings of the armour and inner cooling pipe into the discretised image space i.e. curved volumes into voxels. It is useful to validate this process by comparing the calculated volumes from the prescribed dimensions with the volumes measured by counting voxels assigned to each part. This is shown in Table 8.

Table 8. Dimensions and expected volume of each monoblock section according to design. OD = outer diameter, ID = inner diameter, l = length.

	Dimensions (mm)	Geometric Volume (mm^3)	Voxel count	Segmented Volume (mm^3)
W	Cuboid with pipe bore (22 x 22 x 4) – (ID = 14, l = 4)	1320	31384394	1390
CuCrZr	Pipe OD = 12, ID = 10, l = 4.5	156	6941170	156
Interlayer (foam + pores)	Pipe OD = 14, ID = 12, l = 4	163	4230825	151
Total		1639	42556389	1697

4.3 FE mesh generation

4.3.1 In silico experiment: laser flash analysis

The accuracy of the meshing to represent the graphite foam was first verified by calculating the porosity of the 'cut' LFA samples. This was accomplished by measuring the FE mesh volumes for the graphite foam samples from nodal coordinates and comparing these against the porosity of the segmented image in the locality of the surrounding region of interest. This is an informative check because the original image data is discretised into cuboids (voxels) and during meshing smoothing operations are performed to better represent the curved surfaces of the real material. These results are shown in Table 9.

Table 9. Comparison of porosity of segmented image region of interest with FE mesh of sample.

LFA sample (name denotes axis and location)	Porosity from raw image data in cuboid sub-volume around LFA disc sample (%)	Porosity within LFA disc sample after conversion to finite elements (%)
Xlow	64.49	64.32
Xcentre	64.80	64.66
Xhigh	64.13	63.97
Ylow	63.73	63.56
Ycentre	64.81	64.66
Yhigh	63.72	63.56
Zlow	64.59	64.45
Zcentre	64.75	64.59
Zhigh	64.05	63.90
Average	64.34	64.19
Standard Deviation	0.418	0.422

4.3.2 Case study: Fusion energy heat exchanger component

The volume of the meshed monoblock model can be checked against the values in Table 8 for further dimensional changes from the original data introduced at the meshing stage, this is shown in Table 10. Additionally, Table 10 contains further analysis of the parts' geometries showing measured surface areas and the calculated ratio between volume and area.

Table 10. Statistical analysis of monoblock FE mesh geometries from CT image.

	Element count	Volume (mm^3)	Surface area (mm^2)	Ratio (area/volume)
W	2646130	1390	1220	0.9
CuCrZr	785241	157	386	2.5
Pores	2451773	115	838	7.3
Foam	1042211	34	611	18.0
Total	6925355	1697		

4.4 Simulation

4.4.1 In silico experiment: laser flash analysis

Firstly, it is worth considering the CAD models to validate the methodology of calculating thermal conductivity by simulating the LFA experiment. Figure 17 a) shows the temperature rise on the rear face of the sample as would be measured by an infra-red camera in an experimental setup. To facilitate visual comparison of the half-rise time it is convenient to normalise the temperature variation between the sample's initial and maximum temperatures as shown in Figure 17 b).

For the IBFEM models there was a negligible difference in the results of the samples taken from the same plane (e.g. xlow, xcentre and xhigh). For clarity in the data, only the results from the 'centre' samples of each plane are shown (i.e. xcentre, ycentre and zcentre). Figure 18 shows the normalised temperature rise on the rear surface of the samples using the material properties for a) $C_{graphite}$ and b) $C_{avg\_graphite}$. The thermal characterisation values derived from these curves are shown in Table 11. The error was calculated as the difference between the result and the expected value.

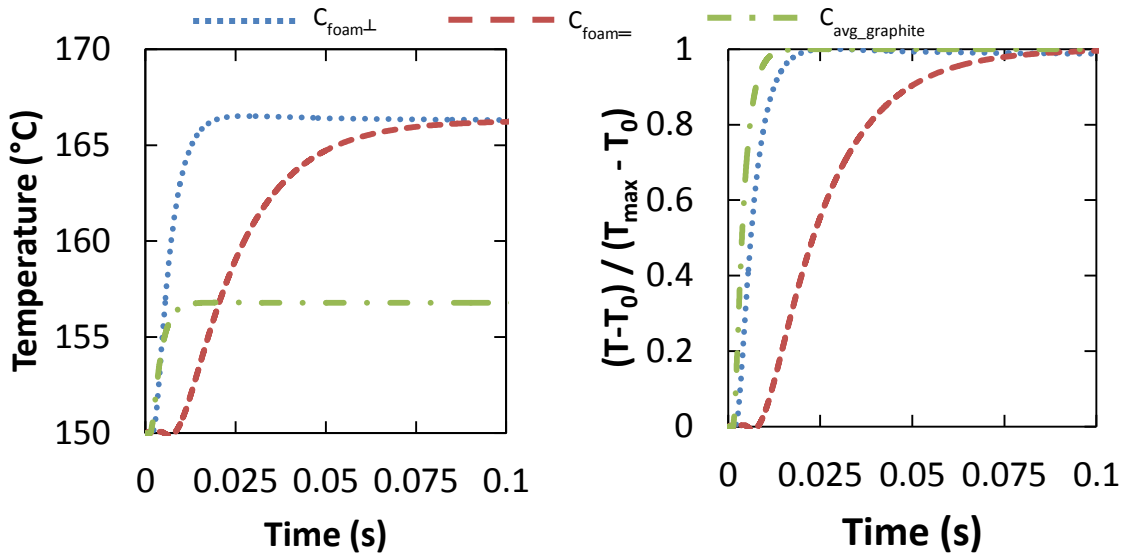

Figure 17. a) Absolute and b) normalised temperature rise on rear surface of solid CAD-based LFA models.

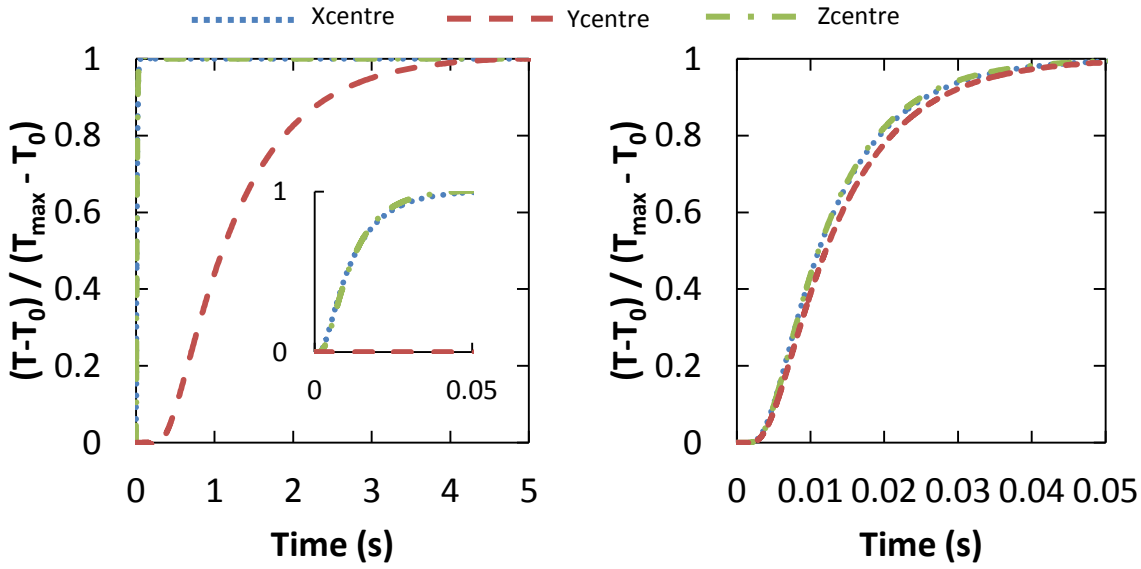

Figure 18. Normalised temperature rise on rear surface of IBFEM samples using the material properties for a) $C_{graphite}$ and b) $C_{avg\_graphite}$.

Table 11. Measured and calculated results from LFA simulation of solid CAD samples.

		Half-rise time (s)	Thermal diffusivity x 10^{-3} (m^2/s)	Effective thermal conductivity (W/m•K)	Error (%)	Measured dT (°C)	Calculated dT (°C)
CAD	$C_{foam\perp}$	0.005858	0.379	247	2.9	16.29	16.27
	$C_{foam=}$	0.022798	0.097	63.4	-0.94	16.28	16.27
	$C_{avg\_graphite}$	0.003488	0.637	993	1.5	6.8	6.79
IBFEM $C_{graphite}$	Xcentre	0.010390	0.283	248	3.3	14.50	14.28
	Ycentre	1.107000	0.00265	2.37	-96	14.19	14.19
	Zcentre	0.009970	0.295	245	2.1	14.47	14.18
IBFEM $C_{avg\_graphite}$	Xcentre	0.011110	0.264	231	-3.8	14.28	14.28
	Ycentre	0.012060	0.243	209	227	14.19	14.19
	Zcentre	0.011070	0.265	234	-2.5	14.19	14.18

4.4.2 Case study: Fusion energy heat exchanger component

The following results demonstrate the use of IBFEM with a component simulated under in-service conditions. Figure 19 shows a comparison front view of the temperature on the surface of the monoblock once steady state had been reached for the three simulations performed ($CAD_{anisotropic}$, $CAD_{isotropic}$ and IBFEM). The second row of images is focussed closer on the material interface region with temperature bounds rescaled to show additional information. Despite primarily providing qualitative data, it is helpful to visualise the temperature contours resultant from the thermal flux applied to the plasma facing surface and heat sink in the coolant pipe.

In order to obtain quantitative data from these models a temperature profile was taken through the monoblock. The path was drawn from the centre of the bottom surface to the centre of the plasma facing surface, as shown in Figure 20. The results for each model are combined in Figure 21, which also notes the change in material along the path (shown along the lower horizontal axis). Figure 22 shows the temperature for the point at the end of this path (i.e. on the plasma facing surface) with respect to time.

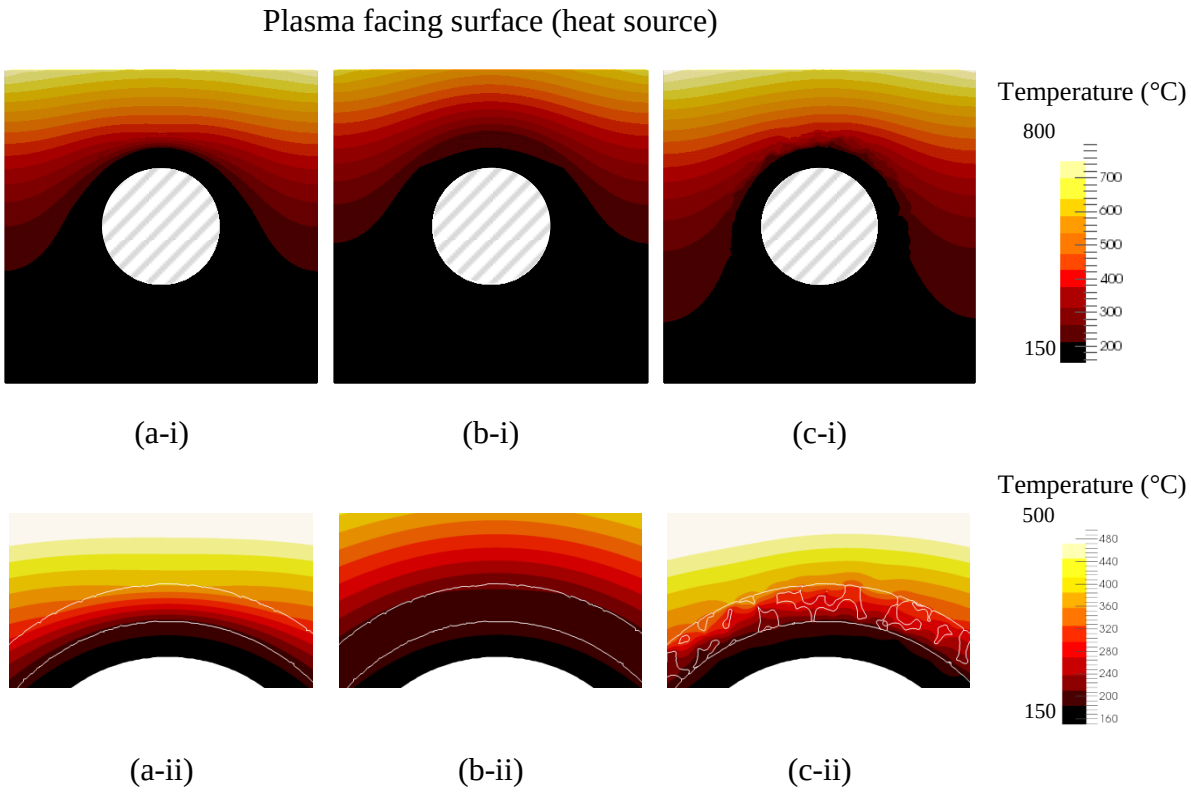

Figure 19. Temperature contour map on front view of monoblock once steady state had been reached for (a) $CAD_{anisotropic}$, (b) $CAD_{isotropic}$ and (c) IBFEM simulations.

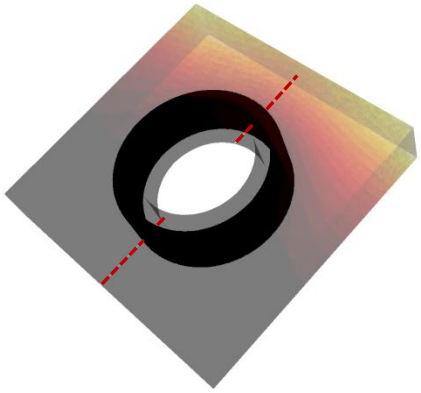

Figure 20. Visualisation of monoblock (armour and pipe sections semi-transparent) to show temperature profile path.

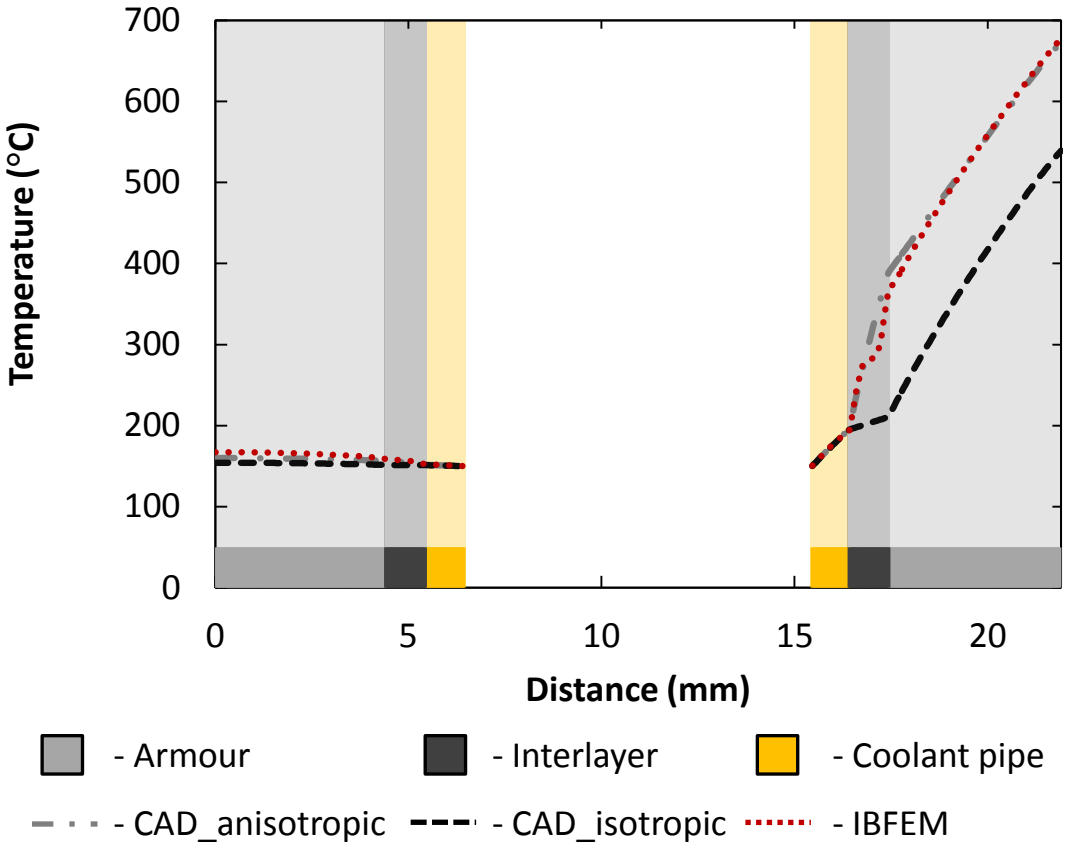

Figure 21. Temperature profile along path shown in Figure 20 for all three models once equilibrium was reached (also denoting material section along the lower horizontal axis).

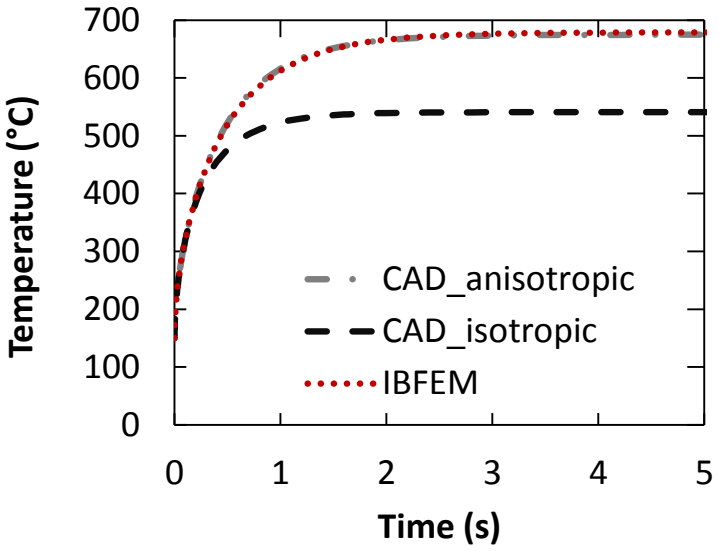

Figure 22. Temperature rise with respect to time at the centre of the plasma facing surface (i.e. end point of profile path in Figure 20).

5 Discussion

5.1 X-ray computerised tomography (CT) scanning

The manufacturer states that the average wall thickness in the graphite foam is 348 μm. Because the X-ray tomography setup used here yields a voxel width of 35.4 μm it is appropriately suited to accurately image the foam. The image provides an average of 10 voxels across the wall thickness.

5.2 Image post-processing

It can be seen that the values for porosity and density calculated from the processed image are comparable to within ~2% of those cited elsewhere (also shown in Table 6). This indicates that the digitisation of the foam on a microstructural level is an accurate representation.

When considering the variation of tortuosity with respect to changing orientation clear trends can be seen. As the azimuthal angle, θ, varies from 0° to 90°, tortuosity decreases from ~1.25 to 1.1 at the midpoint of 45°, then increases back to its original peak similar to 2π of a cosine curve. For variation in the polar angle, ϕ, from -90° to +90° a similar behaviour is observed from peaks of ~1.22 to troughs of 1.18, but with three peaks emulating 4π of a cosine curve. It should be noted that the peak at 0° has a higher value of 1.26. The averaged values along the Cartesian axes show that the tortuosity in the x and z axes are similar to each other to within 1.5 %. However, the average tortuosity is ~6.6 % higher along the y-axis. This would indicate that the thermal conductivity would be lower in the xz plane, i.e. in the direction the foam was 'grown' during manufacture, compared to the perpendicular planes. The observed values agree with the manufacturer's measured values, Table 1. Despite being a useful indicator, measuring the tortuosity alone is not sufficient for estimating the change in effective thermal conductivity from that of the parent material. For example, multiplying the tortuosity value with that of the original values for graphite underestimates reduction in conductivity. This is an oversimplification of heat transfer, omitting mechanisms such as heat flow rates or heat losses. Image-based modelling will account for the cross-sectional areas of the flow channels through accurate topological representation and therefore better approximate the effective change.

For the image created from the CAD-IBFEM hybrid monoblock, the values for the calculated image volumes and prescribed CAD dimensions are comparable. The volumes of the inner CuCrZr pipe are identical however there is a small difference in both the armour and

interlayer volumes. This is due to operations performed at the armour-interlayer interface to convert curved geometries into voxel data (cuboids) which have caused an overall change in outer diameter of the interlayer. The voxels for this image are cubes with a side length of 35.4 μm, therefore incorrectly determining the interlayer or armour dimensions by one voxel would result in a volumetric change of 3.1 mm^3 or 23 mm^3, respectively. From the variation in expected and resultant volumes it can be calculated that the interlayer outer diameter is 13.87 mm rather than 14 mm. For this work, this level of divergence from design is not of importance as the main aim is to relatively compare the results for the CAD and IBFEM simulations (which use the same mesh and therefore have the same dimensions).

5.3 FE mesh generation

5.3.1 In silico experiment: laser flash analysis

One metric to indicate consistency in volume is to compare the porosity of the segmented 3D image data with that of the FE mesh. It can be seen that there is very little change with the LFA samples; the FE mesh porosity values are 4.6% lower than those for the whole block of graphite foam, shown in Table 6, which is likely due to the whole block containing the 3.2 mm layer at the bottom with a different microstructure where pores can be observed to be significantly larger, see Figure 11.

5.3.2 Case study: Fusion energy heat exchanger component

For the monoblock, the agreement between volumes for the segmented image and FE mesh is very good, any differences are negligible. As can be expected, the area to volume ratio is lowest for the armour and highest for the foam interlayer due to its fine microstructure. These ratios demonstrate that microstructural detail in the graphite foam have been retained during meshing.

Measuring the mesh quality shows that the meshes do contain some elements outside the desired quality thresholds for the in-out and edge length aspect ratios. However these are only a very small percentage of the overall mesh (~0.0008%) and all elements are within acceptable limits for the other metrics. Given the fine resolution of the meshes these are unlikely to have a significant effect on the global results other than in extremely localised regions. Considering the mean and worst values for mesh quality it can be observed that the meshes are of adequate quality for FE purposes.

5.4 Simulation

5.4.1 In silico experiment: laser flash analysis

Firstly we will consider the results of the CAD-based LFA samples. By comparing the thermal conductivity values calculated from the simulation results (see Table 11) with the original values that were input as the models' material properties (see Table 5), there is good agreement for all three samples (i.e. regardless of anisotropy in material properties). The difference between these values was less than 3 %. Additionally the samples' final temperatures match the values calculated analytically very closely. This demonstrates that it is possible to calculate a disc shaped sample's thermal conductivity by simulating the LFA experiment and processing simulation results in the same way as their experimental counterparts.

Having established confidence in the methodology for CAD simulations it is then appropriate to evaluate the results of the IBFEM simulations. The fact that there was a high level of repeatability for samples digitally 'cut' from the same plane shows that there was a suitably large representative volume to exhibit the effective bulk behaviour in that plane.

For both sets of simulations, using the $C_{graphite}$ then $C_{avg\_graphite}$ material properties, the temperature rise curves (see Figure 18) and derived values (see Table 11) of the Xcentre and Zcentre samples are similar. The alignment of these samples from the yz and xy planes are equivalent to that of the CAD $C_{foam\perp}$ where the manufacturer's stated effective thermal conductivity is 240 W/m•K. The foam's input thermal conductivity in the ⊥ orientation for $C_{graphite}$ is 1950 W/m•K and the results show that this reduces to an effective thermal conductivity of 248 and 245 W/m•K for Xcentre and Zcentre, respectively, which is ~3% higher than stated by the manufacturer. For the $C_{avg\_graphite}$ simulations these values reduce to 231 and 234 W/m•K which is 3% lower than the manufacturer's value. That is, the effective thermal conductivity is marginally overestimated when anisotropic material properties are used and underestimated when averaged to be isotropic with the IBFEM model. The differences are of the same order to that observed in the idealised CAD models.

The Ycentre sample was 'cut' from the third orientation, the ═ or xz plane, and is equivalent to that of the CAD $C_{foam=}$ where the manufacturer's stated effective thermal conductivity is 64 W/m•K. For the $C_{graphite}$ and $C_{avg\_graphite}$ simulations the effective thermal conductivity reduces to 2.4 and 209 W/m•K, respectively. These values are significantly different

compared to the manufacturer's values. For the $C_{graphite}$ model this is a logical outcome because the input thermal conductivity in the plane of the thermal path was 5.7 W/m•K, and the effective thermal conductivity can only be lower than this due to the increased thermal path caused by the pores. The input thermal conductivity was already significantly lower than the manufacturer's effective value. Therefore, the observed value from the simulation was expected to be lower than 5.7 W/m•K.

Note that, when comparing the results of each of the planes from the $C_{avg\_graphite}$ models (i.e. isotropic input thermal conductivity), the effective thermal conductivity is lower for Ycentre (═ plane) than Xcentre and Zcentre (⊥ planes). This indicates, as indicated from the preliminary tortuosity analysis, that the anisotropy in effective thermal conductivity is affected by the microstructure. However, because the microstructure alone did not reduce the effective thermal conductivity to the level measured experimentally it appears as through the anisotropy is a combination of the effects of the foam's microstructure and graphite's crystallographic structure. That is, the reality of the anisotropic behaviour is somewhere between the naïve assumption in the $C_{graphite}$ models that the whole foam structure is perfectly aligned with graphitic lattice planes or as in the $C_{avg\_graphite}$ models that the foam is purely amorphous with isotropic properties.

To better understand the relationship between the graphite foam's material properties and effective behaviour the improvement on the law of mixtures suggested by Markworth [36] was used to profile the change in thermal conductivity in the ⊥ and ═ planes, $k_{\perp}$ and $k_{=}$, with respect to the fractional change between a purely crystalline to purely amorphous material, f, as shown in Equation (5) and the profile shown in Figure 23 a).

$$k_e = k_{\perp} \cdot \frac{k_{\perp}(1-f) + k_{=}(1+f)}{k_{\perp}(1+f) + k_{=}(1-f)} \tag{5}$$

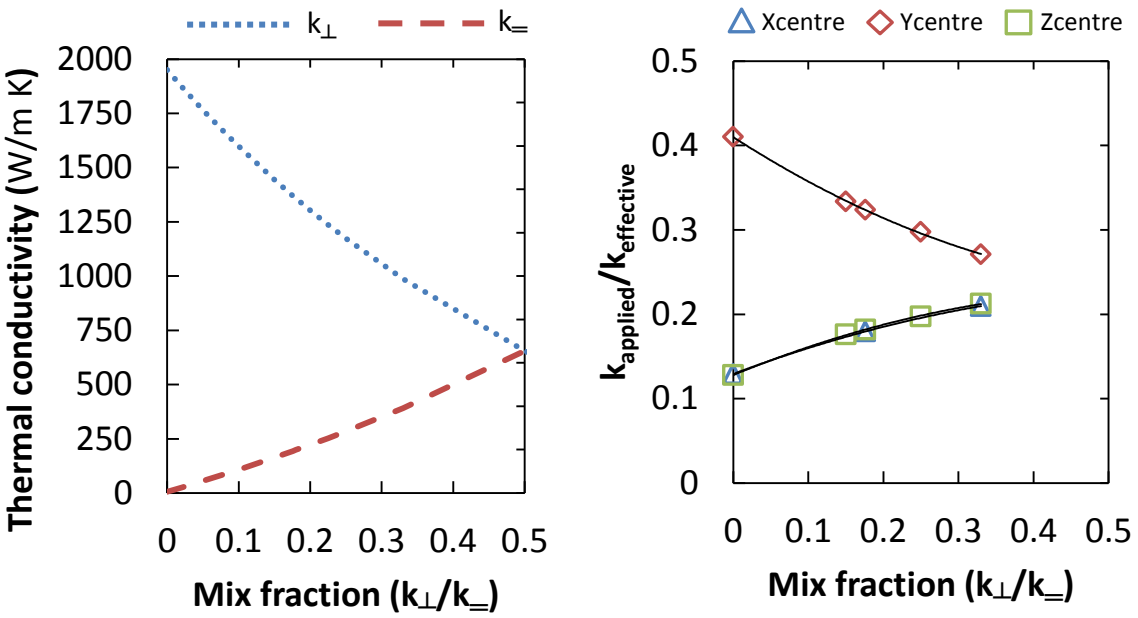

Figure 23. a) Thermal conductivities in the ⊥ and ═ planes with respect to changing mix fraction i.e. from purely crystalline to amorphous. b) Ratio of applied and effective thermal conductivities from IBFEM simulations using $k_{\perp}$ and $k_{=}$ values from a).

Further IBFEM simulations were performed using thermal conductivities derived from the profiles shown in Figure 23 a), taken at various mix fractions. Figure 23 b) shows the ratio of applied and effective thermal conductivities for each mix fraction. Using a second order fit to these results it was predicted that f = 0.176 ($k_{\perp}$ = 1370 and $k_{=}$ = 194 W/m•K) would produce the model with effective thermal conductivities nearest those stated by the manufacturer. This was tested and was found to give effective thermal conductivities of 246 and 249 W/m•K in the yz and xy (⊥) planes, then 63 W/m•K in the xz (═) plane. In this instance, this method has been used here to back calculate the relation between the anisotropy on the crystalline scale. Ideally, a better theoretical understanding of the changes in the crystallographic structure due to manufacturing processes would enable the mix fraction, f, to be identified analytically for a complete in silico characterisation of the effective thermal conductivity.

Given the significant difference between the input and effective thermal conductivities, the degree of accuracy in predicting the effective thermal conductivity, particularly in the ⊥ planes, demonstrates this in silico technique to be a promising method of replacing experimental methods.

5.4.2 Case study: Fusion energy heat exchanger component

In addition to investigating the characterisation of novel materials with in silico experiments it is useful to test their in-service performance within a component to identify the best candidates prior to manufacturing. The case study presented here is included as a demonstration of how the image-based modelling approach may be used instead of CAD-based modelling to investigate this without having measured the material's effective material properties experimentally to be included as input data and, despite this, provide increased accuracy through the inclusion of microstructural detail.

From the images in Figure 19 it can be seen that (a) $CAD_{anisotropi}$ and (c) IBFEM have similar peak temperatures on the plasma facing surface whereas the temperatures on the same surface in (b) $CAD_{isotropic}$ are lower. Despite the previous similarity, the location at which the temperature reaches 200 °C on the thin sides perpendicular to the plasma facing surface is different for each simulation. Considering the distance from the maximum temperatures to the point at which temperature reaches 200 °C, the thermal gradients for the (a) $CAD_{anisotropic}$, (b) $CAD_{isotropic}$, and (c) IBFEM models in respective order are 42,200, 42,900 and 37,600 °C/m. This is of significance because higher thermal gradients indicate higher thermally induced stresses due to non-uniform thermal expansion. The likely reason for the $CAD_{anisotropic}$ and IBFEM models having a greater difference in the ═ plane than ⊥ planes is due to the IBFEM model not sufficiently emulating the mechanisms causing a thermal barrier in that plane, as shown by the LFA simulations.

Another significant difference is the thermal gradient across the armour-interlayer-pipe interfaces. The $CAD_{anisotropic}$ model, shown in Figure 19 (a), has a steep thermal gradient from the low temperature of the pipe to the higher temperature of the armour whereas in the $CAD_{isotropic}$ model, shown in Figure 19 (b), the thermal gradient is more gradual. The IBFEM model has a highly non-uniform transition over the material interface region, with visible localised 'hot spots' (seen more clearly in Figure 19 (c-ii). The non-uniformity and non-symmetry observed in the IBFEM model (not seen in either CAD model) have been introduced by the non-uniform geometries included when modelling the graphite foam on the microstructural level.

Figure 21 and Figure 22 show that the maximum temperature for the $CAD_{isotropic}$ model is significantly lower than that of the $CAD_{anisotropic}$ or IBFEM models. This is due to the significantly lower thermal gradient in the interlayer section between the pipe and the plasma

facing surface for $CAD_{isotropic}$ than the other two models. Therefore, despite a similar gradient through the pipe and armour regions, the plasma facing surface experiences a maximum temperature of 539 °C rather than 673 °C for the $CAD_{anisotropic}$ and IBFEM models, a difference of 20 %. The $CAD_{isotropic}$ model doesn't take into consideration the anisotropy of graphite or the foam microstructure, therefore it can be concluded that using the material properties for graphite averaged over the planes for a solid interlayer overestimates the thermal conductivity. The results for the $CAD_{isotropic}$ are not included to accurately represent the foam interlayer, but rather because they are a useful baseline for comparison of other results.

The main interest here is to compare the $CAD_{anisotropic}$ and IBFEM models to determine whether the new approach of simulating without knowing effective material properties priori gives comparable results to the conventional approach. The $CAD_{anisotropic}$ and IBFEM models show a strong level of agreement despite using a fundamentally different approach to represent material properties for the interlayer. That is, the $CAD_{anisotropic}$ values are for bulk foam properties as measured experimentally and the IBFEM values are theoretical based on combining literature values for carbon with the foam microstructure.

As could be expected, the main difference is the temperature profile through the interlayer region where the models completely differ in their approach. The profile for the IBFEM model fluctuates significantly due to passing through foam and porous phases whereas it is continuous for the homogenised $CAD_{anisotropic}$ model. These are extremely localised fluctuations built into the model, and therefore, when considering the global effect of the interlayers the results are comparable. The second observable difference between the two models is a small variation in temperature on the bottom surface of the monoblock, 154 °C and 167 °C for the $CAD_{anisotropic}$ and IBFEM models respectively. This is again due to too high an effective thermal conductivity in the $=$ plane. The final difference that can be observed is that the IBFEM results aren't perfectly symmetrical as with the $CAD_{anisotropic}$ model. For example, in the temperature contour map shown in Figure 19 the temperature gradient is different on the left hand side of the armour to the right hand side, this is related to the positioning of the foam micro-structures and where they contact the armour to create a thermal path. Although this only causes small global variations, the ability to consider each manufactured part individually may be invaluable for optimising the assembly of a multi-part component. This is a clear benefit over conventional CAD based modelling.

The level of agreement shown in this case study demonstrates the potential benefits and validity of the IBFEM approach with respect to the widely accepted method of homogenising complex microstructures for CAD-based modelling.

- By using literature values for material properties and microstructure alone IBFEM may predict the thermal performance of graphite foam without prior knowledge of its effective bulk performance and without measuring those experimentally. If foam with a new microstructure was produced it would be possible to model it from X-ray CT data without the need to perform a time consuming range of thermal testing. This could be a powerful tool for rapid development of new functional materials.
- The $CAD_{anisotropic}$ model gives a geometrically ideal, and therefore symmetrical, result which may be globally valid but does not provide localised information within the foam. The IBFEM model may be interrogated at smaller scales to investigate local fluctuations resulting from the microstructure which could potentially be significant to the part's structural integrity. Developments underway in this wider field of materials simulation will allow modelling of the structural integrity at an even finer scale by using a multiscale cellular automata – finite element (CAFE) approach [37].
- Finally, the simulation results show strong agreement; differences observed are primarily due to the increased microscale accuracy inherent in the IBFEM model. In scenarios such as this, where microstructure is a significant contributor to performance, additional confidence in predicting performance from a 'digital twin' model of a real part may be of significant operational value if the design is approaching safety limits.

6 Conclusions

Functional carbon based materials with material properties which can be 'tuned' exist that are of interest for high value manufacturing e.g. in nuclear applications. Some of these materials have complex anisotropic micro-structures which influence the effective (bulk) material properties. It is often simple to modify these micro-structures during manufacturing to change the material properties, but experimentally characterising the new effective performance is often time-consuming and expensive. This work presented a technique to perform characterisation experiments in silico by digitising novel materials via X-ray tomography to enable virtual testing with the image-based finite element method (IBFEM). By accounting for micro-structure to predict effective performance, the simulation only requires knowledge

of the parent material which only needs characterising once. This may therefore be used to expedite the development of functional materials by assisting downselection of candidate materials. Presented here was an example that investigated the thermal conductivity of a graphite foam by simulating laser flash analysis.

In this particular example it was observed that the effective thermal conductivity was caused by a combination of the graphite foam's microstructure and crystallographic structure. There was insufficient data about the crystallographic structure. Consequently, the assumptions made about input material properties were too simplistic to predict the effective material properties in all orientations with a high degree of accuracy. Using literature values for the material property of graphite, the foam's effective thermal conductivity was predicted to be 250 and 2.3 W/m•K in the ⊥ and ═ plane, respectively. The difference between input and effective thermal conductivity was due to thermal barriers caused by the extended thermal path between one surface of the sample to the other. The graphite foam manufacturer's values, measured experimentally, were 240 and 64 W/m•K. By using the law of mixtures it was possible to adjust the input thermal conductivity such that the effective values matched those of the manufacturer. Presently, the required mix fraction was found empirically meaning increased understanding of the crystallographic structure is needed. Therefore, this study demonstrated that this use of IBFEM as a tool to predict effective material properties shows promise but that its effectiveness depends on the level of detailed knowledge about the parent material. Its use with less complex materials such as metals may be more appropriate.

This work then demonstrated how the image-based modelling technique may be used to 'digitally manufacture' a component containing such a functional material to assess its performance under in-service conditions. Doing this in silico reduces the dependency on 'real' manufacturing and potentially logistically challenging experimental testing. A case study was presented where the functional material (graphite foam) was used as part of a heat exchange component, termed monoblock, for a fusion energy device. The other parts of the component were drawn using CAD, thus a hybrid CAD-IBFEM model was created.

To test the validity of the CAD-IBFEM model its results were compared to a standard CAD models of the same component where the microstructures in the functional material region were homogenised and average material properties assigned. The CAD model used the manufacturer's anisotropic material properties for the graphite foam which were measured experimentally.

The IBFEM model was in good agreement with the CAD version which used the manufacturer's properties. This demonstrated that despite having no prior knowledge of the bulk performance of the graphite foam, faithfully modelling the geometry of the material on the microstructural level yielded results comparable to homogenisation techniques. The advantage of the IBFEM technique is that, in addition to having been shown to increase modelling accuracy for such materials, the model can be interrogated on a more localised level to provide potentially critical additional information.

Although IBFEM has been used in the context of fusion engineering in this work, it could be used in a broad range of applications, particularly where materials with complex behaviours are used and bulk performance may not be easily measured. Ultimately, it is envisaged that IBFEM could be developed for quality assurance on production lines to gain confidence in component integrity, thus either increasing fabrication yields or reducing engineering reserve factors.

7 Acknowledgements

This work has been carried out within the framework of the EUROfusion Consortium and has received funding from the Euratom research and training programme 2014-2018 under grant agreement No 633053 and from the RCUK Energy Programme [grant number EP/I501045]. To obtain further information on the data and models underlying this paper please contact PublicationsManager@ccfe.ac.uk. The views and opinions expressed herein do not necessarily reflect those of the European Commission. This work made use the HPC resources of The Hartree Centre (project fusionFEM) made available within the Distributed European Computing Initiative (DECI-12) by the PRACE-2IP, receiving funding from the European Community's Seventh Framework Programme (FP7/2007-2013) under grant agreement RI-283493. Access to the Archer UK National Supercomputing Service was provided by EPSRC through projects EP/N026136/1 and e515 "GEMS: Geometric Modelling of Solids". Additionally, the authors would like to thank the Manchester X-ray Imaging Facility for use of tomography equipment, which was funded in part by the EPSRC (grants EP/F007906/1, EP/F001452/1 and EP/I02249X/1).

8 References

[1] S. J. Zinkle and J. T. Busby, "Structural materials for fission & fusion energy," *Mater. Today*, vol. 12, no. 11, pp. 12–19, Nov. 2009.

[2] K. L. Murty and I. Charit, “Structural materials for Gen-IV nuclear reactors: Challenges and opportunities,” *J. Nucl. Mater.*, vol. 383, no. 1–2, pp. 189–195, Dec. 2008.

[3] C. P. C. Wong, V. Chernov, A. Kimura, Y. Katoh, N. Morley, T. Muroga, K. W. Song, Y. C. Wu, and M. Zmitko, “ITER-Test blanket module functional materials,” *J. Nucl. Mater.*, vol. 367, pp. 1287–1292, 2007.

[4] F. C. Difilippo, “Neutronics and thermal effects of graphite foams in the performance of nuclear energy systems,” *Ann. Nucl. Energy*, vol. 31, no. 2, pp. 135–149, 2004.

[5] J.-W. Yeh, “Recent progress in high-entropy alloys,” *Ann. Chim. - Sci. des Matériaux*, vol. 31, no. 6, pp. 633–648, 2006.

[6] D. W. Clark, S. J. Zinkle, M. K. Patel, and C. M. Parish, “High temperature ion irradiation effects in MAX phase ceramics,” *Acta Mater.*, vol. 105, pp. 130–146, 2016.

[7] L. L. Snead, T. D. Burchell, and A. L. Qualls, “Strength of neutron-irradiated high-quality 3D carbon fiber composite,” *J. Nucl. Mater.*, vol. 321, no. 2–3, pp. 165–169, Sep. 2003.

[8] G. N. Praveen and J. N. Reddy, “Nonlinear transient thermoelastic analysis of functionally graded ceramic-metal plates,” *Int. J. Solids Struct.*, vol. 35, no. 33, pp. 4457–4476, Nov. 1998.

[9] I. J. Beyerlein, A. Caro, M. J. Demkowicz, N. A. Mara, A. Misra, and B. P. Uberuaga, “Radiation damage tolerant nanomaterials,” *Mater. Today*, vol. 16, no. 11, pp. 443–449, Nov. 2013.

[10] A. S. Kukushkin, H. D. Pacher, V. Kotov, G. W. Pacher, and D. Reiter, “Finalizing the ITER divertor design: The key role of SOLPS modeling,” *Fusion Eng. Des.*, vol. 86, no. 12, pp. 2865–2873, 2011.

[11] R. A. Pitts, A. Kukushkin, A. Loarte, A. Martin, M. Merola, C. E. Kessel, V. Komarov, and M. Shimada, “Status and physics basis of the ITER divertor,” *Phys. Scr.*, vol. T138, no. T138, p. 14001, Dec. 2009.

[12] A. Herrmann, H. Greuner, M. Balden, and H. Bolt, “Design and evaluation of an optimized W/Cu interlayer for W monoblock components,” *Fusion Eng. Des.*, vol. 86, no. 1, pp. 27–32, 2011.

[13] J. H. You, G. Mazzone, E. Visca, C. Bachmann, E. Autissier, T. Barrett, V. Cocilovo, F. Crescenzi, P. K. Domalapally, D. Dongiovanni, S. Entler, G. Federici, P. Frosi, M. Fursdon, H. Greuner, D. Hancock, D. Marzullo, S. McIntosh, A. V. Müller, M. T. Porfiri, G. Ramogida, J. Reiser, M. Richou, M. Rieth, A. Rydzy, R. Villari, and V. Widak, “Conceptual design studies for the European DEMO divertor: Rationale and first results,” *Fusion Eng. Des.*, vol. 109–111, no. PartB, pp. 1598–1603, 2016.

[14] W. Lin, J. Yuan, and B. Sundén, “Review on graphite foam as thermal material for heat exchangers,” *World Renew. Energy Congr. 2011 - Sweden*, pp. 748–755, 2015.

[15] B. E. Thompson, “Heat Transfer in Porous Graphite Foams,” *J. Heat Transfer*, vol. 136, no. 3, p. 32602, Dec. 2013.

[16] J. Sanchez-Coronado and D. D. L. Chung, “Thermomechanical behavior of a graphite foam,” *Carbon N. Y.*, vol. 41, no. 6, pp. 1175–1180, Jan. 2003.

[17] K. C. Leong and H. Y. Li, “Theoretical study of the effective thermal conductivity of graphite foam based on a unit cell model,” *Int. J. Heat Mass Transf.*, vol. 54, no. 25–26, pp. 5491–5496, Dec. 2011.

[18] C. C. Tee, N. Yu, and H. Li, “Modeling the overall heat conductive and convective properties of open-cell graphite foam,” *Model. Simul. Mater. Sci. Eng.*, vol. 16, no. 7, p. 75006, Oct. 2008.

[19] M. K. Alam, A. M. Druma, and C. Druma, “Thermal Transport in Graphitic Carbon Foams,” *J. Compos. Mater.*, vol. 38, no. 22, pp. 1993–2006, Nov. 2004.

[20] J. Schindelin, I. Arganda-Carreras, E. Frise, V. Kaynig, M. Longair, T. Pietzsch, S. Preibisch, C. Rueden, S. Saalfeld, B. Schmid, J.-Y. Tinevez, D. J. White, V. Hartenstein, K. Eliceiri, P. Tomancak, and A. Cardona, “Fiji: an open-source platform for biological-image analysis.,” *Nat. Methods*, vol. 9, no. 7, pp. 676–82, Jun. 2012.

[21] J. Schindelin, C. T. Rueden, M. C. Hiner, and K. W. Eliceiri, “The ImageJ ecosystem: An open platform for biomedical image analysis,” *Mol. Reprod. Dev.*, vol. 82, no. 7–8, pp. 518–529, Jul. 2015.

[22] T. C. Lee, R. L. Kashyap, and C. N. Chu, “Building Skeleton Models via 3-D Medial Surface Axis Thinning Algorithms,” *CVGIP Graph. Model. Image Process.*, vol. 56, no. 6, pp. 462–478, Nov. 1994.

[23] I. Arganda-Carreras, R. Fernández-González, A. Muñoz-Barrutia, and C. Ortiz-De-Solorzano, “3D reconstruction of histological sections: Application to mammary gland tissue,” *Microsc. Res. Tech.*, vol. 73, no. 11, pp. 1019–1029, Oct. 2010.

[24] H. Ye and M. Y. Ma, “An image analysis method to obtain the effective thermal conductivity of metallic foams via a redefined concept of shape factor,” *Appl. Therm. Eng.*, vol. 73, no. 1, pp. 1277–1282, Dec. 2014.

[25] Y.-H. Zhao, Z.-K. Wu, and S.-L. Bai, “Thermal resistance measurement of 3D graphene foam/polymer composite by laser flash analysis,” *Int. J. Heat Mass Transf.*, vol. 101, pp. 470–475, Oct. 2016.

[26] L. Margetts, “Parallel Finite Element Analysis,” University of Manchester, 2002.

[27] I. M. Smith, D. V. Griffiths, and L. Margetts, *Programming the Finite Element Method*, 5th ed. Chichester: Wiley, 2013.

[28] I. M. Smith and L. Margetts, “The convergence variability of parallel iterative solvers,” *Eng. Comput.*, vol. 23, no. 2, pp. 154–165, Feb. 2006.

[29] Ll. M. Evans, L. Margetts, J. Bushell, T. Lowe, A. Wallwork, W. E. Windes, P. Young, and P. M. Mummery, “Parallel processing for time-dependent heat flow problems,” in *NAFEMS World Congress*, 2013.

[30] L. Margetts, L. Mason, J. D. Arregui-Mena, and W. T. Hewitt, “Parallel finite element analysis using the Intel Xeon Phi,” in *EMiT Emerging Technology Conference*, 2016.

[31] Ll. M. Evans, L. Margetts, V. Casalegno, L. Lever, J. Bushell, T. Lowe, A. Wallwork, P. Young, A. Lindemann, M. Schmidt, and P. Mummery, "Transient thermal finite element analysis of CFC–Cu ITER monoblock using X-ray tomography data," *Fusion Eng. Des.*, vol. 100, pp. 100–111, 2015.

[32] J. Blumm and J. Opfermann, "Improvement of the mathematical modeling of flash measurements," *High Temp. - High Press.*, vol. 34, pp. 515–521, 2002.

[33] F. Levrero-Florencio, L. Margetts, E. Sales, S. Xie, K. Manda, and P. Pankaj, "Evaluating the macroscopic yield behaviour of trabecular bone using a nonlinear homogenisation approach," *J. Mech. Behav. Biomed. Mater.*, vol. 61, pp. 384–396, 2016.

[34] A. Qsymah, R. Sharma, Z. Yang, L. Margetts, and P. Mummery, "Micro X-ray computed tomography image-based two-scale homogenisation of ultra high performance fibre reinforced concrete," *Constr. Build. Mater.*, vol. 130, pp. 230–240, Jan. 2017.

[35] W. M. Haynes, *CRC Handbook of Chemistry and Physics, 95th Edition*. CRC Press, 2014.

[36] A. J. Markworth, "The transverse thermal conductivity of a unidirectional fibre composite with fibre-matrix debonding: a calculation based on effective-medium theory," *J. Mater. Sci. Lett.*, vol. 12, no. 19, pp. 1487–1489, 1993.

[37] A. Shterenlikht and L. Margetts, "Three-dimensional cellular automata modelling of cleavage propagation across crystal boundaries in polycrystalline microstructures," *Proc. R. Soc. A Math. Phys. Eng. Sci.*, vol. 471, no. 2177, pp. 20150039–20150039, Apr. 2015.

Supplementary Data

Table 12 lists the results for various methods of measuring mesh ‘quality’ as an average of the nine LFA meshes and separately for each of the monoblock materials. The measures used are well-known metrics. Briefly, in respective order, they measure; the normalised in-sphere radius to circumsphere radius ratio; ratio of longest to shortest edge length; non-regularity of element; how close to equilateral the element is; ratio between element volume and ideal element volume; information on volume, shape and orientation of cell.

By looking in more detail on the individual LFA meshes it is possible to look at the worst elements to determine whether there may be any issues despite the mean quality being acceptable. The results for each of the previous metrics are shown in Table 13, which lists the quality of the very worst element followed by the number outside the acceptable value.

Table 12. Mean values for mesh quality measurement parameters.

	Perfect value (Not achievable)	Acceptable value	LFA	Monoblock			
			Foam	W	CuCrZr	Pores	Foam
In-out aspect ratio	1	0.05	0.8	0.7	0.8	0.8	0.7
Edge length aspect ratio	1	10	1.8	1.8	1.7	1.7	2.0
Angular skew	0	0.95	0.4	0.4	0.4	0.4	0.5
Volume skew	0	0.9999	0.4	0.5	0.3	0.4	0.5
Shape factor	1	0.0001	0.6	0.5	0.7	0.6	0.5
Jacobian	1	0.05	0.6	0.5	0.6	0.6	0.5

Table 13. Value for worst element and number of elements outside acceptable mesh quality values for the LFA models.

	X			Y			Z	
	low	centre	high	low	centre	high	low	centre	high
In-out aspect ratio	0.0340 / 18	0.0360 / 22	0.0300 / 20	0.0280 / 24	0.0370 / 12	0.0330 / 18	0.0340 / 15	0.0430 / 12	0.0330 / 19
Edge length aspect ratio	9.8000 / 0	8.9000 / 0	9.9000 / 0	12.000 / 6	12.000 / 2	11.000 / 3	11.000 / 2	11.000 / 1	10.000 / 1
Angular skew	0.9000 / 0	0.8800 / 0	0.8900 / 0	0.9000 / 0	0.8900 / 0	0.9000 / 0	0.9000 / 0	0.8900 / 0	0.9100 / 0
Volume skew	1.0000 / 0	1.0000 / 0	1.0000 / 0	1.0000 / 0	1.0000 / 0	1.0000 / 0	1.0000 / 0	1.0000 / 0	1.0000 / 0
Shape factor	0.0010 / 0	0.0014 / 0	0.0007 / 0	0.0007 / 0	0.0012 / 0	0.0008 / 0	0.0010 / 0	0.0017 / 0	0.0012 / 0
Jacobian	0.1000 / 0	0.1000 / 0	0.1000 / 0	0.1000 / 0	0.1000 / 0	0.1000 / 0	0.1000 / 0	0.1000 / 0	0.1000 / 0